JGR Oceans

RESEARCH ARTICLE
10.1029/2021JC017408

Transport Barriers and the Retention of *Calanus finmarchicus* on the Lofoten Shelf in Early Spring

Huizi Dong[1], Meng Zhou[1], Ziyuan Hu[2], Zhaoru Zhang[1], Yisen Zhong[1], Sünnje L. Basedow[3], and Walker O. Smith Jr.[1,4]

[1]School of Oceanography, Shanghai Jiao Tong University, Shanghai, China, [2]Jiaozhou Bay National Marine Ecosystem Research Station, Institute of Oceanology, Chinese Academy of Sciences, Qingdao, China, [3]Department of Arctic and Marine Biology, UiT The Arctic University of Norway, Tromsø, Norway, [4]Virginia Institute of Marine Science, William & Mary, Gloucester Point, VA, USA

Key Points:

- We identified a transport barrier along the shelf break, trapping *Calanus finmarchicus* on the Lofoten shelf for 30–70 days in early spring
- The slope current is the primary mechanism of forming the transport barrier for restricting shelf-ocean water and plankton exchange
- An increase in baroclinicity leads to eddy activities to disrupt the barrier and enhance cross-slope plankton transport after early spring

Correspondence to:
M. Zhou,
meng.zhou@sjtu.edu.cn

Citation:
Dong, H., Zhou, M., Hu, Z., Zhang, Z., Zhong, Y., Basedow, S. L., & Smith, W. O. (2021). Transport barriers and the retention of *Calanus finmarchicus* on the Lofoten shelf in early spring. *Journal of Geophysical Research: Oceans*, *126*, e2021JC017408. https://doi.org/10.1029/2021JC017408

Received 31 MAR 2021
Accepted 21 JUL 2021

Abstract Large aggregations of the copepod *Calanus finmarchicus* occur each spring in the shelf-slope-oceanic regions off the Lofoten-Vesterålen Islands where productive fisheries have traditionally supported local economies. The retention and off-shelf transport of populations of *C. finmarchicus* populations were studied by analyzing ocean color remote sensing, satellite altimetry data, and Lagrangian Coherent Structures (LCS) between 2010 and 2019. Our analysis revealed the existence of a transport barrier reoccurring at the shelf break that retains *C. finmarchicus* on the shelf for 30–70 days in the spring when *C. finmarchicus* were seasonally ascending to the surface layer. The analysis of baroclinic and barotropic energy conversions indicated that the topographically steered Norwegian Atlantic Current is the primary mechanism in the formation of the transport barrier, which restricts exchanges of *C. finmarchicus* populations between shelf and oceanic waters. In the mid- to late April, an increase in baroclinicity leads to an increase in mesoscale eddies generated on the shelf break near Lofoten-Vesterålen Islands, breaking down transport barriers and causing off-shelf transport of *C. finmarchicus*. The transport barrier predictably reoccurs in early spring which supports the entrapment of *C. finmarchicus* in the shelf region.

Plain Language Summary Large aggregations of the copepod *Calanus finmarchicus* in the continental shelf and slope areas of northern Norway support commercially exploited fish species. Our analysis of LCS based on satellite sea level height data, revealed a recurring transport barrier along the shelf break off the Lofoten-Vesterålen Islands in the early spring. It coincided with a boundary that limits off-shelf transport of *C. finmarchicus*, as observed by ocean color remote sensing data. Particle tracking analysis further verified that the transport barrier occurred every spring between 2010 and 2019, which restricted cross-slope water exchange. Topographic steering of the Norwegian Atlantic Current was the main cause of maintaining the transport barrier for more than 30 days. After mid- or late April, an increase in instability broke down the barrier, enabling cross-slope transport by mesoscale eddies or meanders. This reoccurring and long-lived transport barrier efficiently retains *C. finmarchicus* populations on the shelf.

1. Introduction

Calanus finmarchicus is the dominant copepod species in the Norwegian Sea, and serves as a key link between primary producers and higher trophic levels (Melle et al., 2014; Planque, 2000). Populations of *Calanus* sp. contribute more than 50% of total mesozooplankton biomass in North Atlantic and Subarctic Seas and are the main prey of several large commercial important fish such as the Northeast Arctic Cod (*Gadus morhua*) and the Norwegian herrings (*Clupea harengus*) (Carstensen et al., 2012; Melle et al., 2014; Planque, 2000). Copepods are also harvested commercially and today is a significant fisheries product (Basedow et al., 2019; Toresen et al., 2019). The main water masses in the northern Norwegian Sea are of coastal and Atlantic origin. The Atlantic Water (AW), carried by the Norwegian Atlantic Slope Current (NwASC) can be distinguished from coastal water by its warm and saline properties (Helland-Hansen & Nansen, 1909). In the shelf-slope area off the coast of northern Norway, large aggregations of *C. finmarchicus* occur and are transported northward by both of the Norwegian Atlantic Slope Current (NwASC) and the Norwegian Coastal Current (NCC) during spring and summer (Sætre & Ljøen, 1971; Sætre & Mork, 1981;

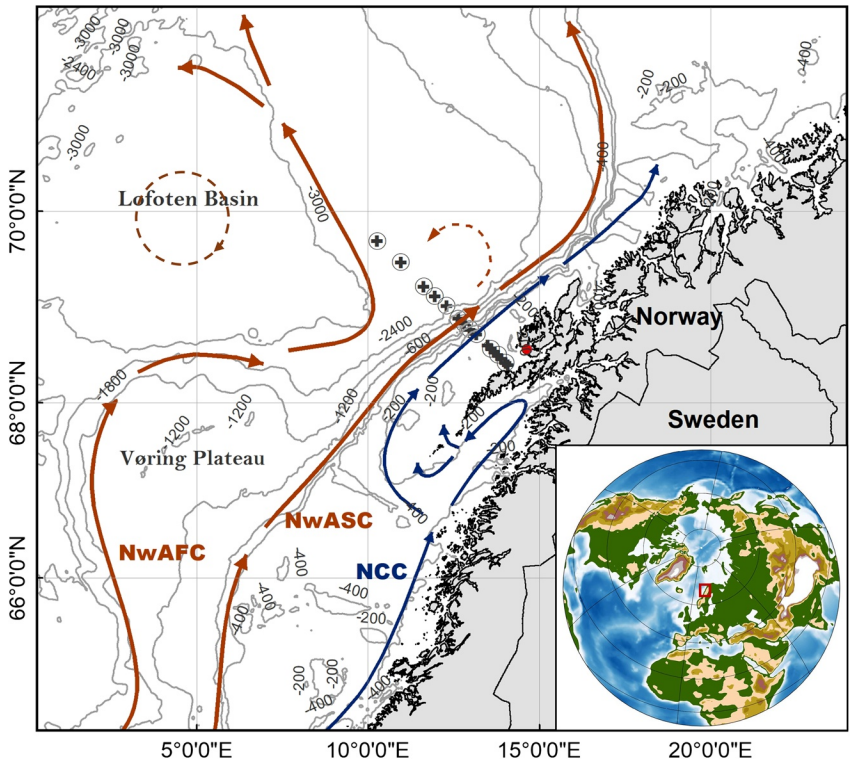

Figure 1. Bathymetry and main currents in the northern Norwegian Sea. Red arrows represent the NwAFC and Norwegian Atlantic Slope Current, and blue arrows represent the Norwegian Coastal Current. The dashed red circle in the Lofoten Basin represents the location of Lofoten Basin Eddy. The black circles and crosses represent the sampling stations during March 20–21, 2019 (Cruise-58UO) and May 22–24, 2019 (Cruise-58JH), respectively. Bathymetry contours are given for every 200 m in areas shallower than 600 m and for every 600 m in areas deeper than 600 m. Location of study area is indicated by the red box in the inset.

Zhu et al., 2009). The complex bottom topography in this area has significant effects on the general circulation pattern, residence time and water mass exchange as well as nutrient transport and plankton aggregations and dispersions (Espinasse et al., 2016; Sætre, 1999; Slagstad & Tande, 1996; Sundby, 1984). The NCC flows along the coast as a wedge-shaped, low-salinity current bordered by the NwASC (Figure 1). A front between NwASC and NCC is usually located near the shelf break (Trodahl & Isachsen, 2018). NwASC is most unstable in the steepest part of the continental slope off the Lofoten-Vesterålen Islands (Isachsen, 2015; Ghaffari et al., 2018). Eddies shed from the NwASC and propagate westward feeding the Lofoten Basin Eddy (LBE), which is stabilized in the Lofoten Basin (LB) by the bottom topography (Bosse et al., 2019; Søiland & Rossby, 2013; Yu et al., 2017).

The biomass and spatiotemporal distributions of *C. finmarchicus* are controlled by reproduction, food availability and predators (Sundby, 2000; Toresen et al., 2019). In early spring, overwintering populations of *C. finmarchicus* migrate from around 1,000 m to the surface, where they mature and spawn (Kaartvedt, 1996). Egg production and hatching success depends on food levels and temperature (Runge et al., 2006). Like other crustaceans, *C. finmarchicus* appears red on the sea surface by synthesizing the carotenoid astaxanthin, which prevents oxidative damage to lipids. Large surface swarms of *C. finmarchicus* in the north Norwegian Sea have been observed from space (Basedow et al., 2019). High abundances of *C. finmarchicus* in surface layers likely influence distributions and migration patterns of their primary predators such as cod and herring. The survival rate during the surface-dwelling period of *C. finmarchicus* is a key factor affecting the overwintering population and the population during the following year (Ohman et al., 2002; Saumweber & Durbin, 2006). However, large-scale climate patterns transmitted throughout the North Atlantic can override local surface processes and may be more important for long-term population size (Weidberg & Basedow, 2019).

Remote sensing technologies of ocean color have been used for phytoplankton biomass estimates, but more recently surface aggregations of high abundances of *C. finmarchicus*, which occur at scales larger than 1,000 km^2, have been observed from space (Basedow et al., 2006, 2019; Bellacicco et al., 2018; McClain, 2009; Liu et al., 2019). This was possible due to the high concentrations of astaxanthin within *C. finmarchicus* individuals, which in turn led to high absorption in the green-blue band. *C. finmarchicus* populations tend to propagate seasonally along and across the shelf break in northern Norway and appear to colonize the mid-Norwegian shelf by utilizing cross-slope currents (Falkenhaug et al., 1997; Halvorsen & Tande, 1999; Slagstad & Tande, 1996). The importance of *C. finmarchicus* in the Norwegian Sea has led to investigations of the physical-biological interactions in the upper ocean, including the role of mesoscale circulations in the habitat, horizontal transport and vertical distributions of zooplankton in the Norwegian Sea (Basedow et al., 2010; Fossheim et al., 2005; Gaardsted et al., 2010; Skarðhamar et al., 2007; Zhou et al., 2009). However, there still is an urgent need to quantitatively study the mechanisms contributing to the formation of *C. finmarchicus* aggregations on continental shelves and exchanges of populations between shelf and oceanic regions.

Transport barriers in the ocean have been investigated with Lagrangian Coherent Structures (LCS) (Alver et al., 2016; Beron-Vera, 2010; Berta et al., 2014; d'Ovidio et al., 2004). Transport barriers have a large impact on coastal environments, not only limiting the exchanges of waters between the two sides of a barrier, but also affecting the distributions of key species in the marine food-web (Enrile et al., 2018; Haller, 2002; Liu et al., 2018; Olascoaga et al., 2008). The use of Finite-size Lyapunov-exponent (FSLE) field maxima to determine LCS has become a valuable tool for visualizing the complex structure of ocean circulation at various spatial and temporal scales (Baudena et al., 2019; De Monte et al., 2012; Prants et al., 2014). LCS analyses have been used to predict the transport of contaminants (such as oil spills), as well as to help understand the dynamical control on the trophic chain between primary producers (Drouin et al., 2019; Lehahn et al., 2007; Olascoaga et al., 2008; Wei et al., 2018) and higher-level predators (Della Penna et al., 2015; Tew-Kai et al., 2009; Scales et al., 2018). In this study geostrophic-based LCS analyses, combined with ocean color remote sensing and numerical simulation results, are used to explore the dynamics controlling formation, stability, and breakdown of the transport barrier for *C. finmarchicus* populations on the shelf and off-shelf regions near the Lofoten-Vesterålen Islands.

2. Data and Methods

2.1. Ocean Color Data

Daily Level-2 data of MODIS Aqua and VIIRS Suomi-NPP in the shelf-slope-oceanic study regions between 65° and 71°N near the Lofoten-Vesterålen Islands (Figure 1) were acquired from the NASA Ocean Color archive (https://oceancolor.gsfc.nasa.gov). High concentrations of the pigment astaxanthin, characteristic of *C. finmarchicus*, were characterized by the strong absorptions in the blue and green bands, and weak absorptions in the red band (Basedow et al., 2019). To distinguish the large aggregations of *C. finmarchicus* in the sea using ocean color remote sensing, a threshold of the reflectance (Rrs) in the unit of sr^{-1} was defined in the blue band (430–450 nm) for both MODIS and VIIRS sensors. Areas with Rrs in the blue band less than 0.003 sr^{-1} were identified as being within *C. finmarchicus* patches, whereas Rrs in the band greater than 0.003 sr^{-1} were defined as the areas without *C. finmarchicus* patches. To understand the temporal-spatial distribution characteristics and variations of *C. finmarchicus* in early spring, data from Level-2 MODIS and VIIRS in three visible bands were processed and analyzed for the period between February and May from 2000 to 2019. After georeferencing, RGB composite results were generated from three reflectance channels: 555, 488, and 443 nm, and 551, 486, and 443 nm, from MODIS and VIIRS, respectively (Table 1). Due to the strong absorption in the 488 and 443 nm bands in MODIS, and 486 and 443 nm in VIIRS, distributions of *C. finmarchicus* aggregations can be determined from the red pixel areas in the RGB composite results.

2.2. Satellite Altimetry and Lagrangian Coherent Structures Analyses

Geostrophic currents used to examine surface currents and eddies are derived from the multi-satellite altimeter missions. The daily surface geostrophic velocity field products with the global 1 / 4 × 1 / 4° horizontal resolution were provided by the Copernicus Marine Service Information (CMEMS,

Table 1
Satellite Ocean Color Data Included in the Study

Satellite	Sensor	Product level	Spatial resolution (m)	Central band (nm)			Coverage time (UTC)
				R	*G*	*B*	
Suomi-NPP	VIIRS	Level-2	750	551	486	443	Apr 17, 2019 11:24:00
							Apr, 10 2019 10:18:00
							May 02, 2016 10:36:00
							Mar 21, 2013 11:12:00
Aqua	MODIS	Level-2	500	555	488	443	Apr 05, 2019 11:20:00
							Apr 09, 2018 11:25:00
							Apr 03, 2018 10:25:00
							Apr 29, 2017 11:30:00
							Mar 30, 2017 11:20:00
							Apr 06, 2016 11:55:00
							May 04, 2015 10:30:00
							Mar 16, 2015 11:25:00
							May 06, 2014 10:50:00
							Apr 23, 2014 11:20:00
							Apr 19, 2012 11:10:00
							Apr 22, 2011 11:25:00
							Apr 05, 2010 11:15:00

http://marine.copernicus.eu) for LCS calculations. The Near Real Time (NRT) merged global ocean gridded Absolutions Dynamical Topography (ADT) Level-4 products for 2019, and the Delayed Time (DT) gridded products for years 2010–2018, were used. Details of processing and quality information of all sea level products are available from CMEMS. Although the horizontal two-dimensional surface geostrophic currents do not completely represent the full current field, the geostrophic flow is one of the dominant components at the scales of interest here. Rypina et al. (2012) demonstrated that ageostrophic components such as Ekman currents are the dominant large-scale motion in the open ocean, but its contribution to mesoscale dispersion is relatively less than that of geostrophic currents. Other ageostrophic components, such as the tides and surface waves, are not considered here either as they are high-frequency signals and on the timescale of copepod transport, their integrated effects turn out to be negligible. Moreover, results from satellite altimetry data and ocean color data can have better co-relationships between datasets produced by observations avoiding uncertainties in three-dimensional models.

Transport properties of a flow field can be described in terms of hyperbolic points and manifolds of the LCS theory (d'Ovidio et al., 2004; Haller & Yuan, 2000; Koh & Legras, 2002; Shadden et al., 2005). The LCS provides the mechanisms explaining coherent convergence and divergence patterns of Lagrangian transport in an unsteady two-dimensional incompressible flow. The computation of Finite-Size Lyapunov Exponents (FSLE) gives a solution for identifying attracting LCS that approximate unstable manifolds (Boffetta et al., 2001; Haller, 2001, 2002; Hu & Zhou, 2019; Shadden et al., 2005). Specifically, the FSLE is defined as:

$$\lambda = \frac{1}{\tau}\log\left(\frac{\delta_f}{\delta_i}\right), \tag{1}$$

where λ is the local measure of the largest exponential separation rate of particle pairs from an initial distance δ_i to a target final distance δ_f after a time interval τ. Trajectories were constructed by integrating the altimetry-based geostrophic velocity field, and employing the fourth-order Runge-Kutta integrator method with linear interpolation both in space and in time. FSLE were computed following the methods described in d'Ovidio et al. (2004). The values of δ_i and δ_f affect the identification of LCS in the flow field and depend on the properties of the flow field itself, the length scale of the structure of interest and the size of the field.

Sensitivity analyses of LCS have been performed to find an optimal combination of the two parameters. δ_i affects the visibility of the details and also determines the resolution of the FSLE field, and δ_f influences the detection of the structures. δ_i and δ_f were adopted as 0.02° and 0.4° to appropriately capture the mesoscale and sub-mesoscale structures. The time step was set to be 3 h. The unit of FSLE is in d^{-1}. Lagrangian trajectories were computed backward in time ($\lambda < 0$), which is often considered as an indicator of frontal activity (Della Penna et al., 2015; Scales et al., 2018). Regions with higher absolute values of backward FSLE results represent a strong horizontal convergence (attracting) effect, and the maxima of absolute FSLE values are defined as the most attracting effect of material trajectory patterns in a region (Hu & Zhou, 2019; Olascoaga et al., 2006). The water particles on both sides move closer and accelerate faster along the ridge, but they cannot pass through the ridge to the other side. Such a structure acts as a barrier preventing cross-slope transport over a certain period of time.

2.3. Reanalysis Data and Kinetic Energy

Velocity data from the CMEMS ocean model GLORYS 12v1 were used to analyze mean kinetic energy (MKE), eddy kinetic energy (EKE), and energy conversion between mean flow and eddy fields. Regional MKE and EKE were analyzed to investigate their monthly variations during spring. The GLORYS 12v1 product provides global ocean circulation reanalysis between 1993 and 2018 at the eddy-resolving resolution of 1/12° in horizontal grids with 50 vertical levels. The hydrodynamic model used to generate this data set is based on NEMO3.1, in which in situ observations, along-track altimetry data and ocean color remote sensing products are assimilated. The atmospheric forcing comes from the ERA-Interim product.

MKE and EKE are estimated as:

$$\mathrm{MKE} = \frac{1}{2}\left(\overline{u}^2 + \overline{v}^2\right), \tag{2}$$

$$\mathrm{EKE} = \frac{1}{2}\left(u'^2 + v'^2\right), \tag{3}$$

where u and v are the zonal and meridional velocities. The overbar denotes the monthly mean, and the prime denotes the deviation from the monthly mean. MKE refers to the kinetic energy in monthly averaged flow, associated with large-scale movements, whereas the EKE refers to the deviation from this mean state and associated with mesoscale processes.

2.4. Analysis of Energy Conversion Rate

Based on the GLORYS 12v1 product, the energy conversion rates between mean flow and eddy fields were analyzed. The baroclinic conversion rate (BC) and the barotropic conversion rate (BT) were used to estimate the energy conversion between the mean potential energy (MPE) and the eddy potential energy (EPE), inferring the trend of baroclinic instability of currents, and the energy conversion between the MKE and the EKE inferring the trend of mean current barotropic instability (Fer et al., 2020; Li et al., 2020; von Appen et al., 2016). The energy conversion rates in both fields gave a solution to understand the transport barrier formation and disruption mechanisms. BC and BT are calculated as:

$$\mathrm{BC} = g\,\overline{v'\rho'}\frac{\partial z}{\partial y}, \tag{4}$$

$$\mathrm{BT} = -\rho_0\overline{u'v'}\frac{\partial \overline{u}}{\partial y}, \tag{5}$$

where ρ' is the density deviation, $\rho_0 = 1{,}027$ kg m^{-3} and is a reference density, and $\overline{u}$ is the horizontal mean current in the along-slope direction. u' and v' are the velocity deviations in the along-slope (42° from the East) and across-slope directions respectively, and $\partial z / \partial y$ is the mean isopycnal slope calculated as $\left(\partial\overline{\rho} / \partial y\right) / \left(\partial\overline{\rho} / \partial z\right)$. All temporal averaging was conducted using 15-day moving average; the conversion

rates were calculated in the upper 250 m. When BC or BT are positive, the energy is converted from the mean flow to the eddy field, and vice versa. If BC > 0, MPE converts to EPE; if BC < 0, EPE converts to MPE. Similarly, if BT > 0, MKE converts to EKE; if BT < 0, EKE converts to MKE.

2.5. Hydrographic Data Set

Hydrographic data were obtained from the International Council for the Exploration of the Sea (https://www.ices.dk/) database. Stations were sampled using a Seabird conductivity-temperature-depth (CTD) system on a transect with 12 stations in Cruise-58UO between March 20 and 21, 2019 and with 16 stations in Cruise-58JH between May 22 and 24, 2019 (Figure 1). Salinity and temperature data were collected continuously from the sea surface to depths greater than 400 m. Salinity and temperature data from the same transects in March and May in previous years were also analyzed. This transect spans the continental shelf, slope and open ocean off the Lofoten-Vesterålen Islands.

3. Results

3.1. A Transport Barrier Identified by FSLE

The FSLE fields computed from the satellite altimetry data and the RGB composite images from ocean color remote sensing data on April 5, 10, and 17, 2019 suggest the occurrence of a transport barrier near the shelf break (Figure 2). A transport barrier from 67.2°N, 8.9°E to 69.3°N, 13.9°E along the shelf break occurred and separated the red patch containing *C. finmarchicus* on the shelf from the clear open ocean on April 5, 2019 (Figures 2a and 2d). On April 10, a small disturbance of the barrier appeared in the area near 69.0°N, 12.5°E, and offshore transport of *C. finmarchicus* across the slope was indicated by the red patch extending off the shelf (Figure 2b). On April 17, the disturbance became larger and the transport barrier had been disrupted (Figure 2f). Simultaneously, abundant *C. finmarchicus* appeared to be transported off the shelf to the open ocean (Figure 2c).

The geostrophic current fields on April 5, 10, and 17, 2019 illustrate the patterns of forming and breaking processes of the transport barrier (Figure 3). A strong northeastward flow along the shelf break is revealed from the geostrophic current velocity field on April 5, 2019 (Figure 3a). With the gradually weakening of the flow, an off-shelf flow was observed on April 17, 2019 in the area between 68.5° and 70.5°N, 12.0° and 14.5°E (Figure 3c), corresponding to the cross-slope transport of the red patch observed by satellite (Figure 2c).

3.2. Particle Tracking Analysis During Transport Barrier Period

To confirm the role of the strong northeastward current at the slope as a barrier preventing *C. finmarchicus* from being transported off-shelf in early spring, particles released in the zooplankton aggregation area were advected backward to identify their origin locations and trajectories of water parcels from the origins to the aggregation area on April 5, 2019. Particles were released at six selected locations on both sides of the shelf break region (Figure 4a), where the strongest barrier existed. 69 particles were seeded in each box colored in blue and black in the region near the transport barrier, and 77 particles were seeded in each box colored in green and red in the region away from the transport barrier. Particles released on the shelf side near the transport barrier (in black) remained on the shelf for 30 days, and particles released on the open ocean side near the transport barrier (in blue) traveled along the slope without crossing the transport barrier during the same period (Figure 4). Water parcels on both sides of the barrier moved northeastward, and closer to the barrier due to the horizontal convergence associated with the FSLE ridge. In contrast, particles released far away from the transport barrier (in green and red) often crossed the slope. As a result, in the Lofoten shelf and slope region, *C. finmarchicus* originating from coastal areas remained on the continental shelf and aggregated onshore of the transport barrier. The strong slope current acting as a transport barrier revealed by the LCS results prevented across-slope water parcel exchange and thus drove mass horizontal convergence on both sides of the transport barrier.

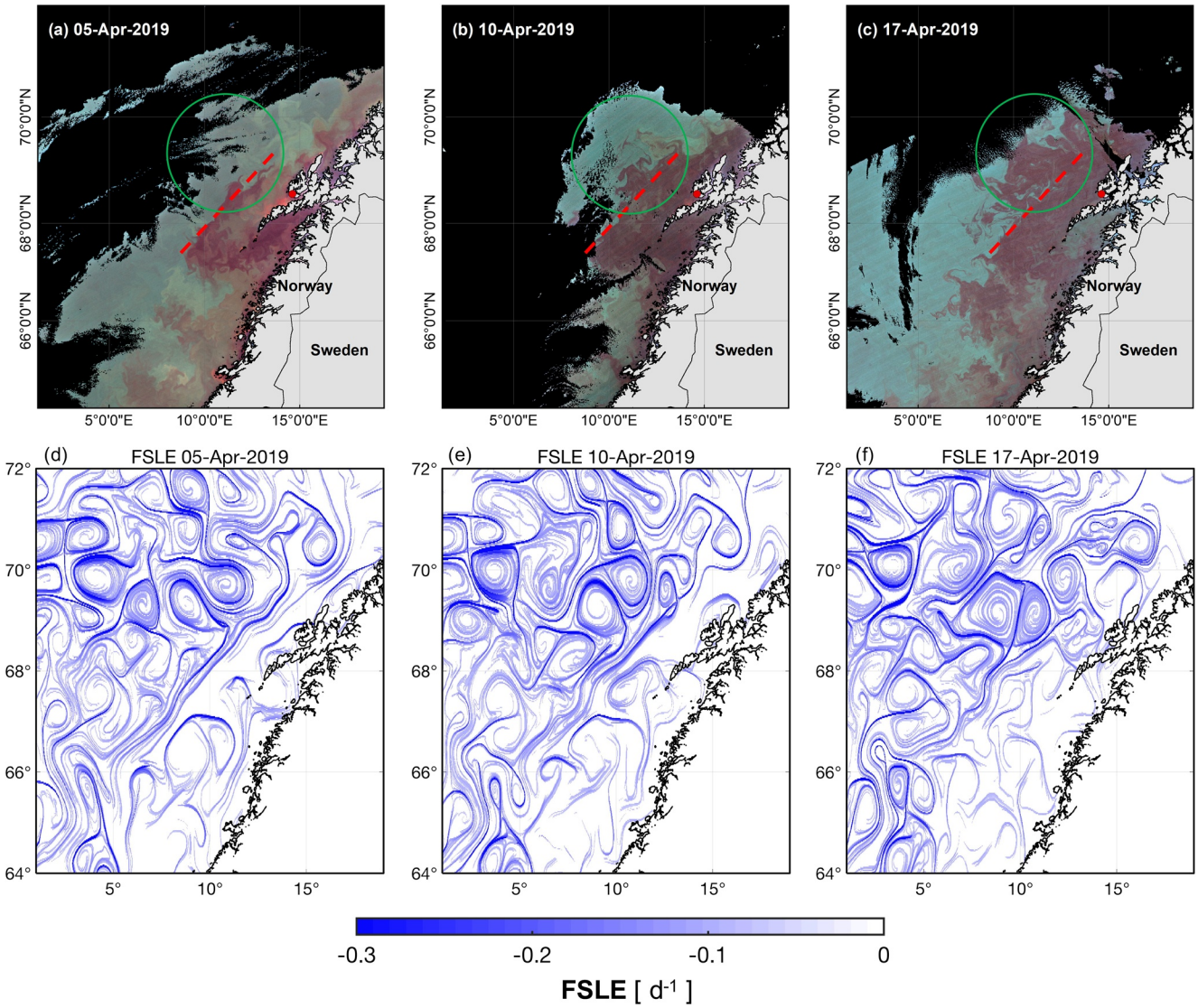

Figure 2. Ocean color images on April 5 (a), April 10 (b), and April 17 (c), 2019. The FSLE (d^{-1}) fields of the same days are shown in (d)–(f), respectively. Dashed red line in (a)–(c) represents the potential transport barrier shown in Figure 2d. The region inside the green circle represents the potential cross-slope transport of *C. finmarchicus* on April 17.

3.3. Particle Tracking Analysis and the Origin of Water Parcels

To track the origin of different water parcels that finally reached the barrier region, four groups of particles were released on April 17, 2019 in the region off the continental shelf in the LCS. In the 30-days FSLE simulation from March 18 to April 17, particles in Group 1 and Group 2 indicate the water parcels transported by NCC traveling northeastward on the Lofoten shelf and NwASC traveling along the Lofoten slope parallel to the NCC along the isobaths (Figure 5a). Particles in Group 3 and Group 4 indicate the paths of water parcels that originated from the Vøring Plateau and the Lofoten Basin. In addition, particles in Group 1 traveled along the shelf break above the Lofoten shelf, and then were transported across the slope around 68.6°N, 12.0°E, which corresponded to the locations of off-shelf movement of *C. finmarchicus* on the same day (Figure 5c). These results suggested that water parcels carrying high abundances of *C. finmarchicus* were transported northward along the shelf break while the transport barrier remained in place (before April 10), but were transported from the shelf to the open ocean when the barrier was disrupted (after April 10).

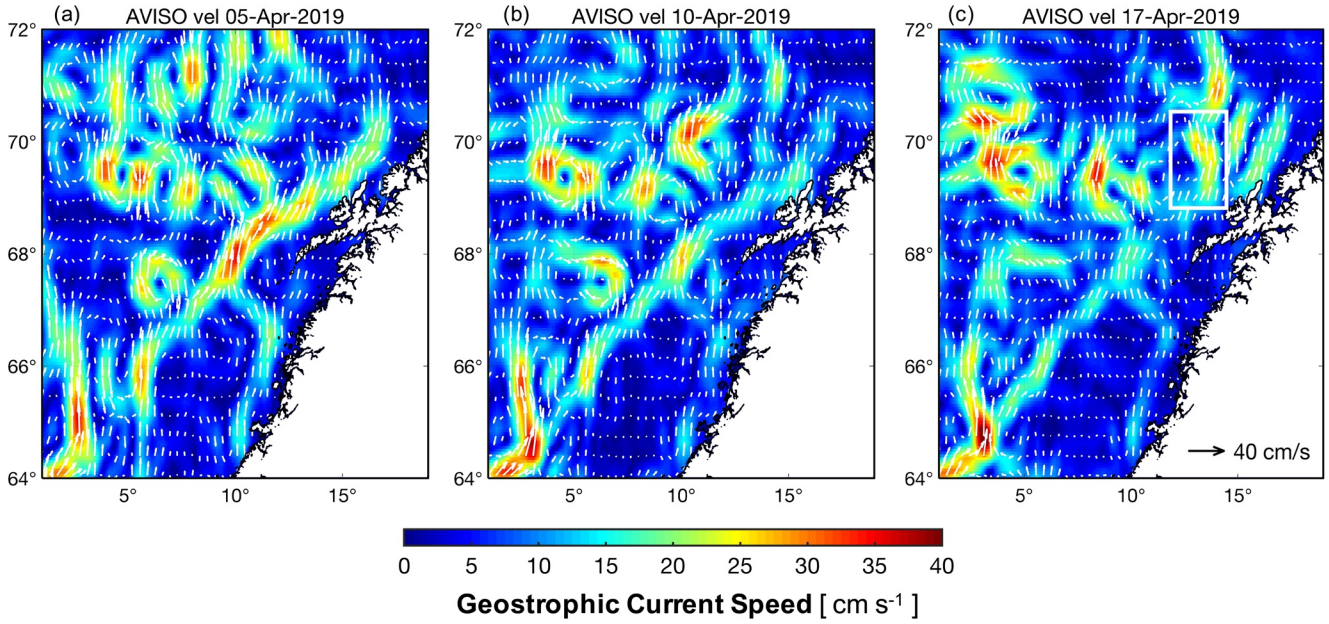

Figure 3. (a–c) are the geostrophic current velocity fields (vectors) on April 5, 10, and 17, 2019 respectively. The color indicates the current speed.

3.4. The Existence of the Spring Transport Barrier Over the Past Decade

Remote sensing data from February to May between 2010 and 2019 were analyzed to determine the existence of transport barriers in spring in different years and its relationship with elevated *C. finmarchicus* abundances, as well as the relationship of barrier breaking with the spatial dispersion of *C. finmarchicus* distributions. Only years with more than 10 satellite images reflecting the distribution of *C. finmarchicus* were analyzed.

During this 10-year period, red patches containing *C. finmarchicus* reoccurred on the Lofoten shelf and lasted between late February and April, suggesting that transport barriers are a common spring feature in the region (Figure 6). From late April to May, the red patch spread from the shelf to the open ocean in all years, suggesting that the breakdown of the transport barrier efficiently carried *C. finmarchicus* across the shelf break to the slope (Figure 7).

To quantify the longevity of the barrier, analyses of both remote sensing and the FSLE data were conducted. The criteria that we used to determine the longevity of the transport barrier from FSLE results were: (a) a transport barrier occurs along the shelf break with the backward FSLE value below $-0.15\ d^{-1}$; (b) the transport barrier is parallel to the slope isobaths (around 42° from East) in the region of 67°–69.5°N off the Lofoten-Vesterålen Islands; and (c) the barrier remains stable for more than 30 days or is only temporarily destroyed for less than 5 days. The criteria to determine the longevity of the transport barrier identified in ocean color remote sensing images, was the presence of a transport barrier for more than 30 days in all available data from February to May. This estimation of the longevity of the transport barrier indicated that the transport barrier maintained and trapped *C. finmarchicus* on the Lofoten shelf for more than 30 days in all of the examined years (Table 2). In 2011 and 2013, large populations of *C. finmarchicus* were trapped on the Lofoten shelf for up to 60 days.

3.5. Vertical Hydrographic Structure in Presence of the Transport Barrier

The Norwegian Coastal Water (NCW) occupied the shelf and was identified by low salinities (<34.8) and temperatures (<6°C; Figures 8a–8f). The Norwegian Atlantic Water (NwAW), with temperatures above 6°C and salinity above 35, extended to a depth of 700 m. Its core flows northward parallel to the NCC along the shelf break. A sharp front with the isohalines of around 6°C and isotherms of around 35 was noted at Stations S7–S9 of Cruise-58UO at depths from 0 to 200 m in March 2019. This frontal structure corresponds

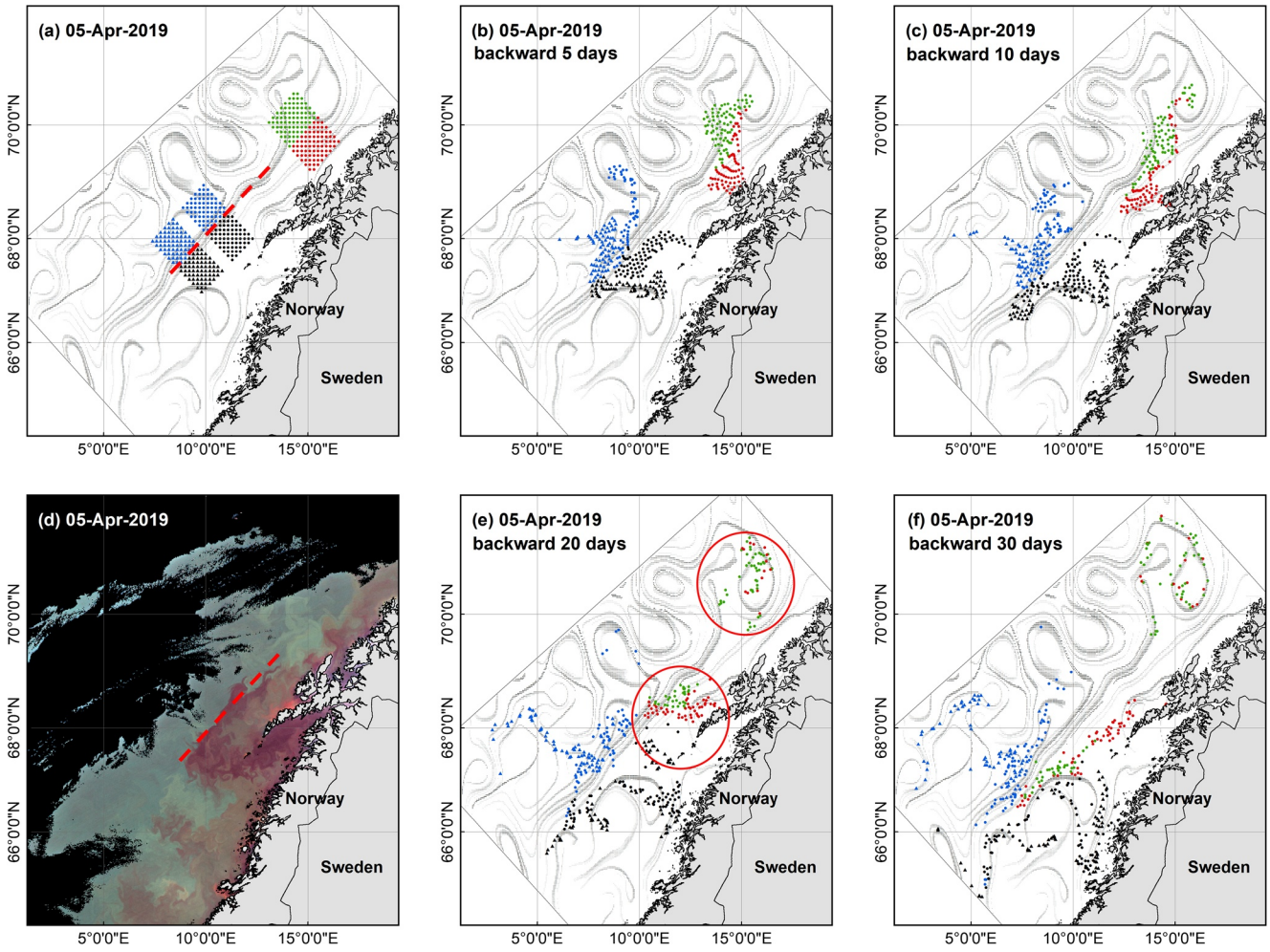

Figure 4. (a) Locations of water parcels released in the backward Lagrangian Coherent Structures (LCS) analyses on April 5, 2019; the black and blue dots and triangles represent the water parcels on the shelf and ocean sides of the potential transport barrier, respectively; the red and green dots represent the water parcels on the shelf and ocean sides in the area away from the transport barrier. The parcel locations at the time of 5, 10, 20, and 30 days prior to April 5, 2019, namely March 31, 26, 16, and 6, are presented in (b), (c), (e), and (f), respectively. The gray curves represent the attracting LCS ridges on April 5, 2019.

to the position of the transport barrier and the boundary of the *C. finmarchicus* on-shelf distributions, suggesting that frontal dynamics may be responsible for regulating the existence and demise of the barrier. During Cruise-58JH the salinity front extended seaward near 69.5°N (near Station S15; Figure 8a) with the off-shelf transport of fresher water. Such a signal further illustrates the process of barrier breaking and mass transport from the shelf to the open ocean.

The colored points in the T-S diagram show different water masses, including NCW, NwAW, and the mixed waters, from stations occupied in March and May 2019 (Figure 8b). The results from shelf stations occupied in March 2019 during the transport barrier period show a nearly linear relationship between temperature and salinity. Mixed waters were found at stations sampled in May 2019 after the transport barrier had broken. For the mixed waters, in the salinity range less than 35.15, the temperature variations were minimal. A mixed water can also be identified by its temperature greater than 6°C resulted from a mixture between NwAW and NCW across the fronts along with the influence of solar radiation on the surface sea water.

3.6. Energy Conversion Between Mean flow and Eddy Fields

The transport barrier dynamics was examined by analyzing the kinetic energy and energy conversion between mean flow and eddy fields. As described in Section 2, MKE refers to the kinetic energy in monthly

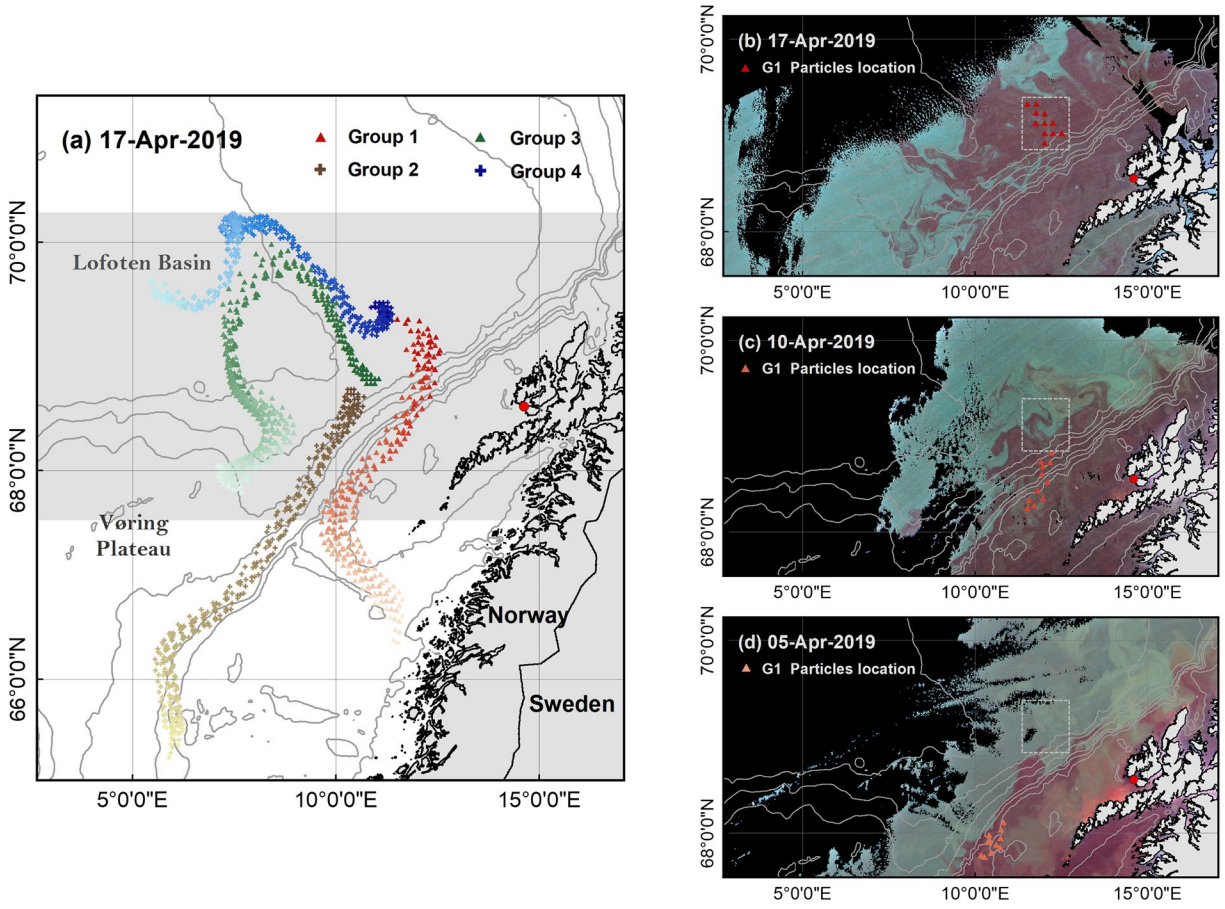

Figure 5. (a) Paths and sources of the water masses indicated by the Lagrangian Coherent Structures (LCS) particle tracking simulation over 30 days. Four groups of particles represent water masses from different dynamical regions separated by the LCS. The darkest color in each group indicates the current location of water mass on April 17, and the lighter color indicates the earlier location in each group during the backward 30 days (b)–(d) show the positions of particles of Group 1 on April 17, 10, and 15, overlying the corresponding remotely sensed *C. finmarchicus* distributions. The dashed white box in (b)–(d) record the particle locations of Group 1 on April 17. Bathymetry contours are shown in gray.

averaged flow associated with large-scale movements, whereas EKE refers to the deviation from this mean state, and is associated with mesoscale processes (Figure 9). High MKE values were found in the region between 600 and 1,000 m isobaths. Along the slope, MKE in February and March was larger than that in April and May, with the maximum reaching 900 $cm^2\ s^{-2}$. In April, enhanced eddy activities weakened the mean flow of the current and MKE was reduced, and in May MKE decreased to below 600 $cm^2\ s^{-2}$. The locations of long-lived transport barriers were estimated by LCS and remote sensing (Figure 10a), corresponding to the locations with higher MKE values in February and March along the slope. For the 10 years analyzed, the disruption of transport barriers and across-slope transport occurred in April, corresponding to the appearance of high EKE in April on the shelf break marked by the dashed red circle (Figures 10a and 10b). The increase in EKE in April led to the increase in cross-slope transport and mixing by mesoscale eddies or meanders as the transport barrier is weakened and eventually broken.

To further understand the barrier formation and disruption mechanisms, the baroclinic conversion rate (BC) and barotropic conversion rate (BT) were used to estimate the energy conversion rate between the mean flow and eddy fields. The calculation was performed at a location within the high EKE area (red circle; Figure 10b). Both BC and BT in February and March are negative, suggesting energy conversion from the eddy field to the mean flow (Figures 11a and 11b). In April, both BC and BT become positive, suggesting the energy is converted from the mean flow to the eddy field due to enhancement in baroclinic and barotropic instabilities. After May, BC dominates and transfers energy from baroclinic MPE to EPE, maintaining the vigorous mesoscale eddies by baroclinic instability.

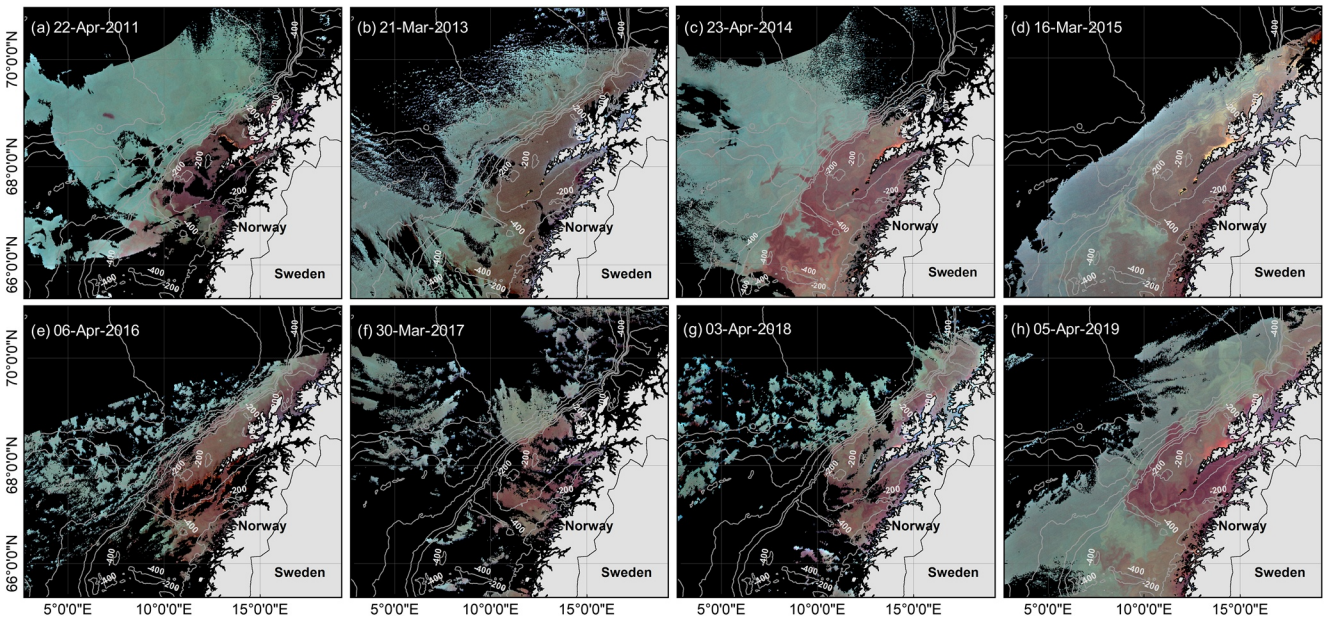

Figure 6. *C. finmarchicus* distributions on the Lofoten shelf in early spring from 2010 to 2019.

4. Discussion

4.1. Impact of Transport Barriers on the Distribution of *C. finmarchicus*

The first *C. finmarchicus* aggregations were observed on the shelf on February 21 (data not shown). The sequence of remote sensing images suggested that plankton populations were trapped on the Lofoten shelf for more than 40 days during spring of 2019. *C. finmarchicus* migrates from their diapause depth (~1,000 m) and aggregates in the surface layer of the continental shelf to feed in the more productive shelf water, thus maximizing their growth and reproduction between February and April. The diapause for overwintering *Calanus* sp. population ends by early February (Heath, 1999; Melle et al., 2014; Opdal & Vikebø, 2015), so

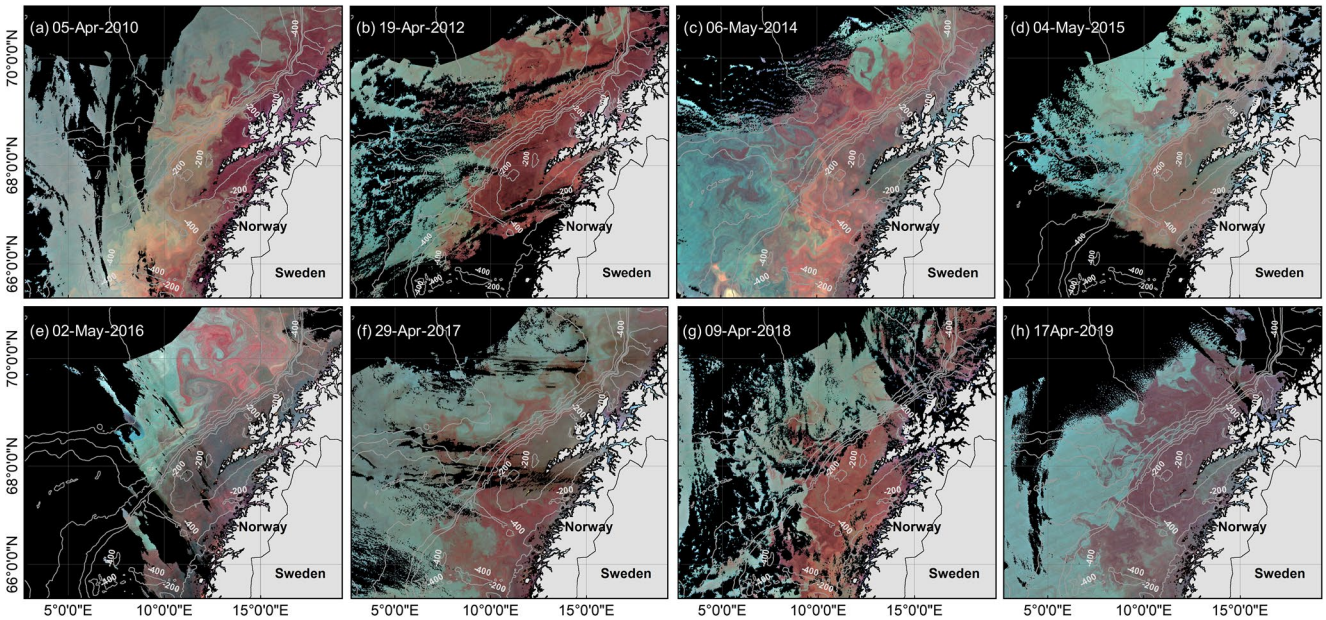

Figure 7. *C. finmarchicus* distributions from Lofoten shelf to the open ocean after early spring from 2010 to 2019.

Table 2
Estimate of the Duration of Transport Barrier Occurrence on the Lofoten Shelf From 2010 to 2019 (STD = Standard Deviation)

Year	2010	2011	2012	2013	2014	2015	2016	2017	2018	2019	Mean ± STD
Barrier duration (days)	32	70	45	63	57	40	45	46	39	48	49 ± 12

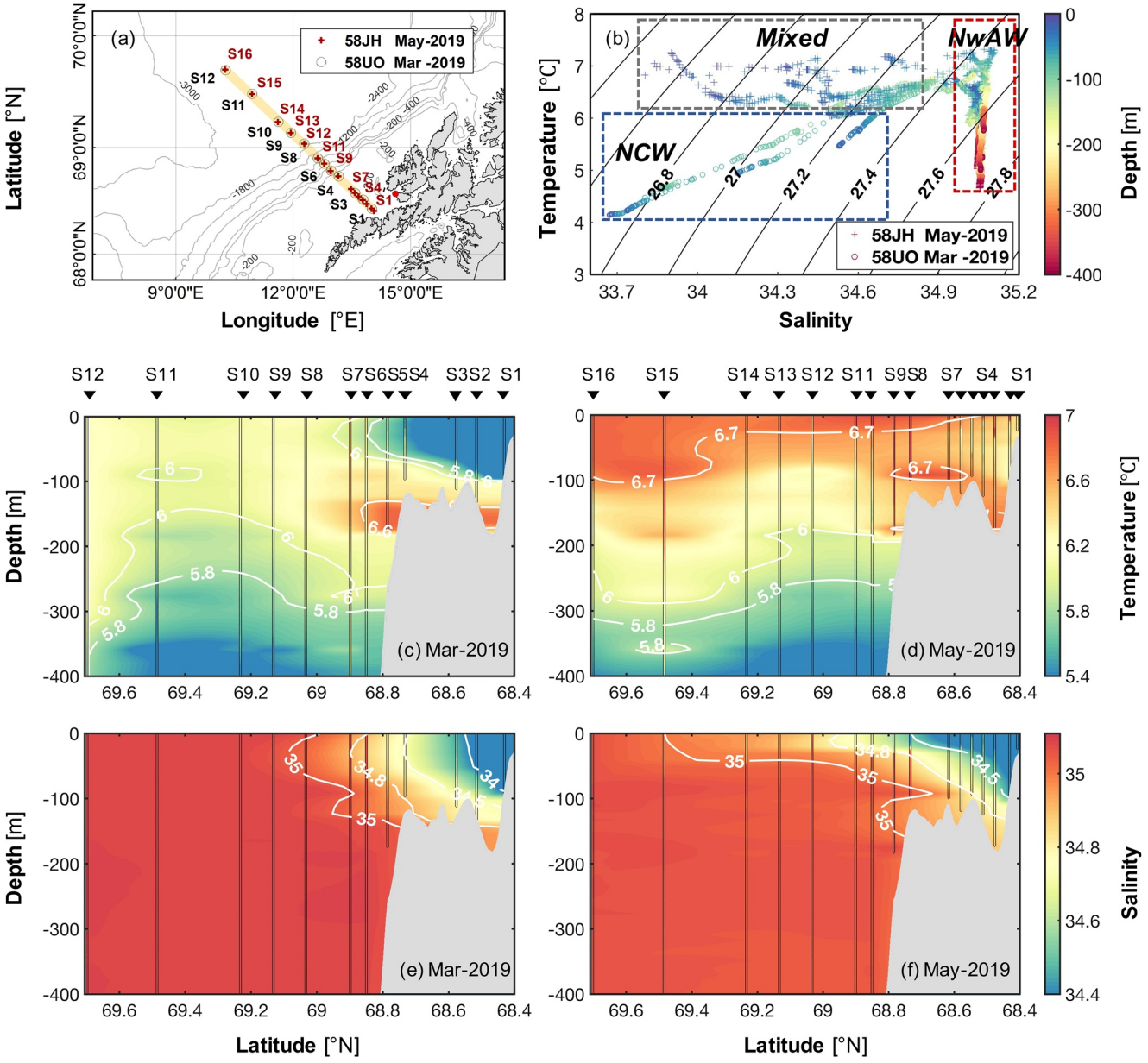

Figure 8. (a) Two transect locations occupied during the study. Black circles represent the sampling stations between March 20, 2019 and March 21, 2019 (Cruise-58UO), red crosses represent the sampling stations during May 22–24, 2019 (Cruise-58JH), and yellow line represents the location of the two transects in March and May 2019. (b) T-S diagram of CTD stations in the transect are colored with the sampling depth, and sampling stations of Cruise-58UO in March marked by crosses and those of Cruise-58JH in May 2019 marked by circles. (c) and (e) Vertical transects of temperature and salinity (0–400 m depth) during the survey in March 2019. (d) and (f) Vertical transects of temperature and salinity (0–400 m depth) during the survey in May 2019.

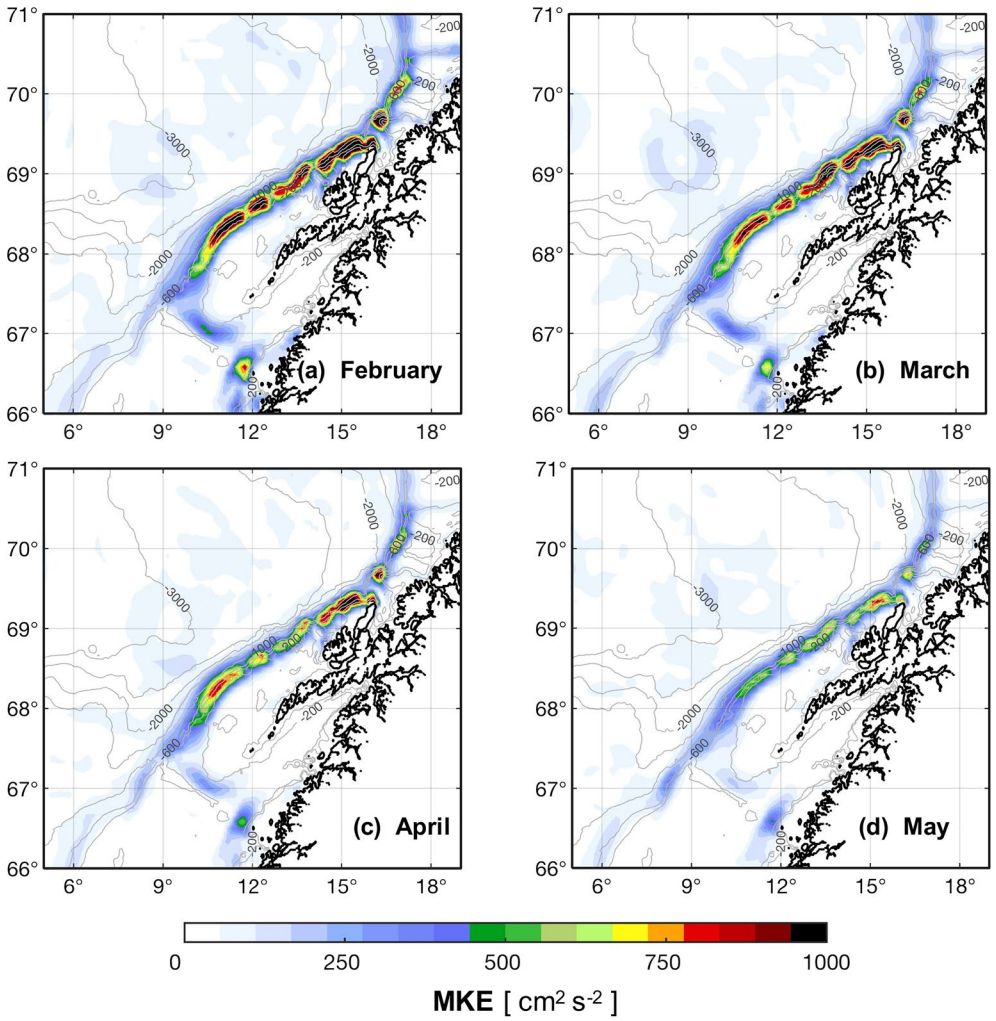

Figure 9. Monthly mean kinetic energy (MKE) averaged from 2010 to 2019 in the upper 250 m in February (a), March (b), April (c), and May (d).

that migration from more than 600 m at 20 m d^{-1} to near surface depth is consistent with their late February appearance. After entering the surface layer, they presumably start to feed and grow (Basedow et al., 2014; Fossheim et al., 2005; Gaardsted et al., 2010; Zhou et al., 2009). Combined with the FSLE field on April 5, a barrier structure along the shelf break occurred that acted as a transport barrier to prevent *C. finmarchicus* from being transported off the shelf (Figure 2d). The spatiotemporal evolution of the barrier from April 5, 10 to April 17 on the shelf break demonstrates the barrier's structure changing from being maintained, to being disturbed, and finally being destroyed (Figures 2d–2f). The distributions of *C. finmarchicus* suggest the cross-slope transport was minimized as a result of the barrier evolution processes (Figures 2a–2c).

4.2. Impacts of the Longevity of Transport Barriers on *C. finmarchicus* Population

Barriers preventing cross-slope mass transport occurred every year between 2010 and 2019 for a period of ~30–70 days in the early spring (Figures 6 and 10a; Table 2). In late April and May, disruption of the barrier results in the off-shelf transport of plankton. For the oceanic *C. finmarchicus* population, this can potentially reduce the impact of predation by higher trophic levels such as developing cod larvae. On the other hand, the spatio-temporal overlap of *Calanus* sp. with developing cod larvae on the shelf over a prolonged period might provide favorable feeding conditions for cod larvae. It is well known that the large stock of Norwegian spring-spawning herring and cod use *C. finmarchicus* as their main prey (Espinasse et al., 2016; Toresen

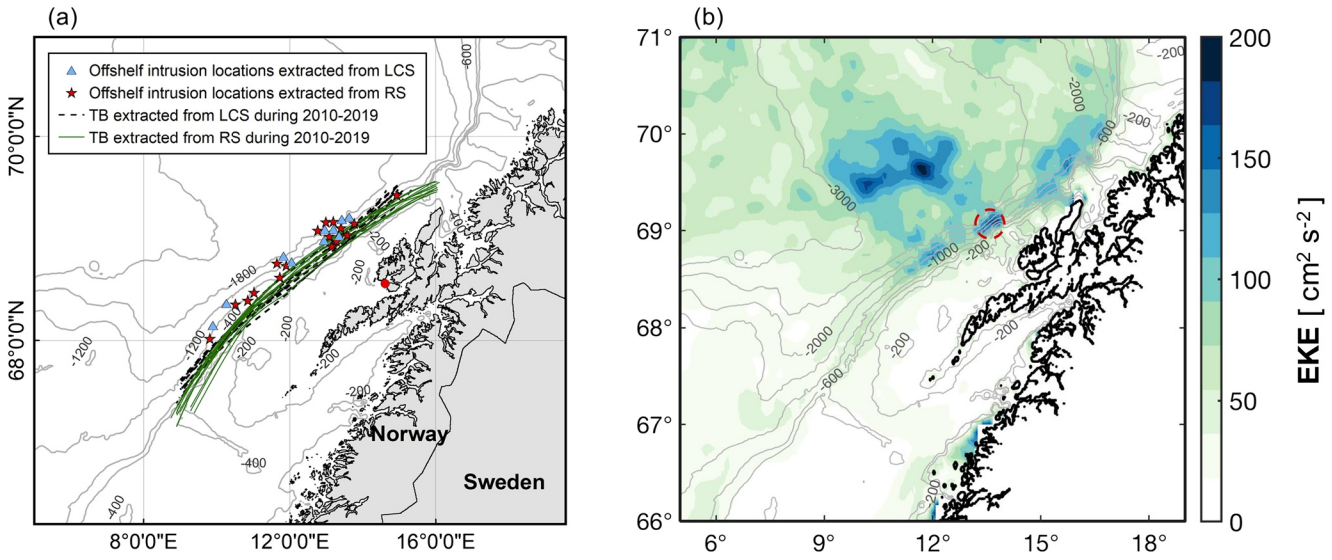

Figure 10. (a) The locations of the transport barrier (TB) extracted by Lagrangian Coherent Structures colored in dashed black line and by Remote Sensing (RS) colored in green line during 2010–2019; the triangles and stars represent the initial cross-slope transport locations off the continental shelf at the end of the TB occurrence during the years 2010–2019. (b) Mean eddy kinetic energy in April during 2010–2019.

et al., 2019). The long-lived transport barrier thus not only affects transport and retention of *C. finmarchicus* populations, but also directly affects future fisheries yields, and influences management including *C. finmarchicus* commercially harvesting and resource conservation.

4.3. Mechanisms of Transport Barriers Formation and Disruption

The MKE results of monthly averages show that the strong MKE was concentrated at the locations of transport barriers in the NwASC path, as expected. The NwASC possesses the highest MKE, and the strength of the NwASC decreases as the season progresses. This indicates that more mean energy is concentrated on the slope during the period of transport barriers, balancing the disturbance of eddies. A strong eddy signal shifting from slope to the northwest of the slope was noted (Figure 10b), suggesting that the eddy is removing the energy of the mean current and leading to the disruption of the transport barrier. The energy conversion results indicate that topographic steering plays a significant role in stabilizing the mean current and incorporating eddy energy into the mean flow (Figure 11). The stable mean current at the slope acts as a mechanism to restrict the shelf-ocean water exchange and forms the persistent transport barrier. During the transport barrier period, the sharpness of the front in the shelf break region off Lofoten-Vesterålen Islands reflect a balance between the along-front current by the strong time-mean currents and across-front stirring or disturbance by mesoscale or sub-mesoscale eddies and meanders (Trodahl & Isachsen, 2018).

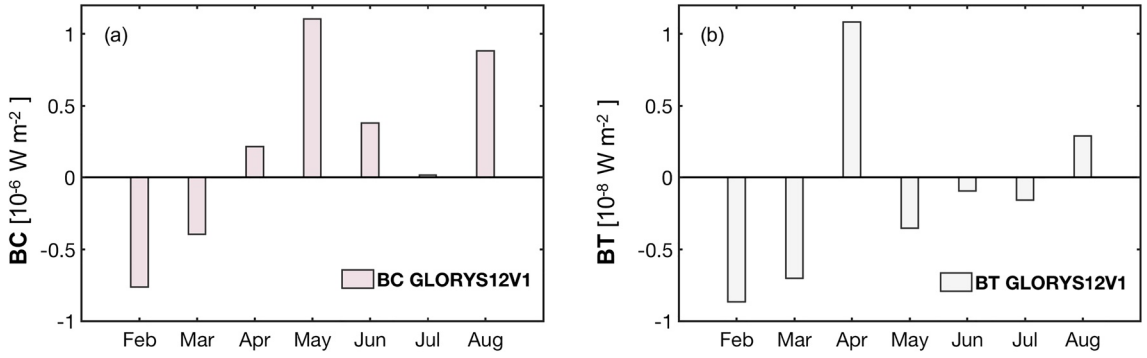

Figure 11. (a) Baroclinic conversion rate (BC) and (b) barotropic conversion rate (BT) between February and August in 2017.

However, the strength of NCC and the wind conditions are also important for stabilizing the transport barrier in early spring. The seasonal lateral displacement of the shelf water due to wind causes the NCC to be deep and narrow in winter and wide and thin in summer (Sætre & Mork, 1981). The seasonal freshwater supply including spring melt and fall precipitation may play a role in breaking the barrier and leading to the *C. finmarchicus* cross-slope transport. The contribution of these terms was not diagnosed in our study.

4.4. The Source of Surface Bloom Populations

C. finmarchicus overwinters at depth in waters off the continental shelf (Kaartvedt, 1996), including the Lofoten Basin and continental slope regions. In addition to the deep-water distribution, fjords are also suitable for *C. finmarchicus* overwintering (Espinasse et al., 2017). Our analysis did not determine the origin of the continental shelf copepod population. For those individuals overwintering in fjord deep waters, once they exit diapause and migrate into the surface layer, the fjord circulation will carry them onto the shelf where they can grow. It is also possible that populations from deeper waters off the shelf may be brought onto the shelf earlier and advected northward with the prevailing coastal current (Figure 1). Finally, temperature-salinity distributions suggest that off-shelf water does indeed penetrate the shelf at depth, which would provide a source of copepods to the Lofoten shelf. Further analyses of winter populations are required to determine the importance of each source as a *C. finmarchicus* seed population (Figure 8).

Other factors may contribute to enhanced copepod biomass during spring on the continental shelf. For example, spring phytoplankton biomass is elevated over the continental shelf relative to oceanic waters, and this in turn would allow *C. finmarchicus* ingestion rates to be greater and foster increased growth. Transport barriers would restrict the physical dissipation of phytoplankton as well as zooplankton, thus providing a near optimal environment for copepod growth. As in all environments, net growth of copepods is a balance between ingestion of food and loss of individuals due to predation, and the relative rates of both in spring are unknow. Regardless, the influence of transport barriers on phytoplankton would be the same as for *C. finmarchicus* and allow the copepod population to maximize its food intake.

5. Conclusions

A transport barrier occurs at the shelf break off the Lofoten-Vesterålen Islands in early spring that significantly affects the transport, retention and distribution of *C. finmarchicus*. Based on the altimetry and ocean color data collected in the past decade, the transport barrier occurred along the shelf break off the Lofoten-Vesterålen Islands in every year, and could retain *C. finmarchicus* on the continental shelf for intervals from 30 to 70 days. The long-term retention of *C. finmarchicus* aggregations on the shelf could directly affect the distribution and production of important predators such as cod and herring as well as phytoplankton.

Disturbances of the barrier caused by meanders or mesoscale eddies lead to cross-slope transport in late spring each year. Three stages occur in the evolution of a barrier: (a) generation of a strong transport barrier preventing plankton from cross-slope transport when a stable barotropic slope current is predominant absorbing EKE into the mean current; (b) a perturbance acting on the barrier when baroclinicity increases; and (c) the formation of mesoscale eddies and meanders when MKE is transferred into eddy kinetic energy. The mesoscale eddy and meander processes play the key role in driving cross-slope transport of *C. finmarchicus* and its large-scale distribution.

Data Availability Statement

The satellite altimetry data were derived from NRT (SEALEVEL_GLO_PHY_L4_NRT_OBSERVATIONS_008_046) and DT data (SEALEVEL_GLO_PHY_L4_REP_OBSERVATIONS_008_047), both of which are freely available from the Copernicus Marine Environmental Monitoring Service (ftp://my.cmems-du.eu/Core/). The reanalysis product GLORYS 12v1 (GLOBAL_REANALYSIS_PHY_001_030) is provided by Copernicus Marine Environmental Monitoring Service (ftp://my.cmems-du.eu/Core/GLOBAL_REANALYSIS_PHY_001_030/). The CTD hydrographic data is provided by ICES (ICES Oceanography data portal, 2012. ICES, Copenhagen) (https://www.ices.dk/). The ocean color remote sensing data

including VIIRS and MODIS was provided by the Ocean Biology Processing Group (https://oceancolor.gsfc.nasa.gov).

Acknowledgments
This work is supported by the Sino-Norway Collaborative STRESSOR Project, funded by the Natural Science Foundation of China (NSFC Grant No. 41861134040) and the Research Council of Norway (RCN Grant No. 287043). This study is also supported by the NSFC Special Program (Grant No. 41941008). The authors acknowledge the captain and crew of R/V *Helmer Hanssen*. The authors thank Professor Francesco d'Ovidio for supporting of LCS. The authors also thank Shengyang Fang for valuable comments and language revisions.

References

Alver, M. O., Broch, O. J., Melle, W., Bagøien, E., & Slagstad, D. (2016). Validation of an Eulerian population model for the marine copepod *Calanus finmarchicus* in the Norwegian Sea. *Journal of Marine Systems*, *160*, 81–93. https://doi.org/10.1016/J.JMARSYS.2016.04.004

Basedow, S. L., Edvardsen, A., & Tande, K. S. (2006). Spatial patterns of surface blooms and recruitment dynamics of *Calanus finmarchicus* in the NE Norwegian Sea. *Journal of Plankton Research*, *28*, 1181–1190. https://doi.org/10.1093/PLANKT/FBL048

Basedow, S. L., McKee, D., Lefering, I., Gislason, A., Daase, M., Trudnowska, E., et al. (2019). Remote sensing of zooplankton swarms. *Scientific Reports*, *9*, 686. https://doi.org/10.1038/S41598-018-37129-X

Basedow, S. L., Tande, K. S., & Stige, L. C. (2010). Habitat selection by a marine copepod during the productive season in the Subarctic. *Marine Ecology Progress Series*, *416*, 165–178. https://doi.org/10.3354/MEPS08754

Basedow, S. L., Zhou, M., & Tande, K. S. (2014). Secondary production at the Polar Front, Barents Sea, August 2007. *Journal of Marine Systems*, *130*, 147–159. https://doi.org/10.1016/J.JMARSYS.2013.07.015

Baudena, A., Ser-Giacomi, E., d'Onofrio, D., Capet, X., Cotté, C., Cherel, Y., & d'Ovidio, F. (2019). *Fine-scale fronts as hotspots of fish aggregation in the open ocean*. BioRxiv. https://doi.org/10.1101/2019.12.16.877571

Bellacicco, M., Volpe, G., Briggs, N., Brando, V., Pitarch, J., Landolfi, A., et al. (2018). Global distribution of non-algal particles from ocean color data and implications for phytoplankton biomass detection. *Geophysical Research Letters*, *45*, 7672–7682. https://doi.org/10.1029/2018GL078185

Beron-Vera, F. J. (2010). Mixing by low- and high-resolution surface geostrophic currents. *Journal of Geophysical Research*, *115*, C10027. https://doi.org/10.1029/2009JC006006

Berta, M., Ursella, L., Nencioli, F., Doglioli, A. M., Petrenko, A. A., & Cosoli, S. (2014). Surface transport in the Northeastern Adriatic Sea from FSLE analysis of HF radar measurements. *Continental Shelf Research*, *77*, 14–23. https://doi.org/10.1016/J.CSR.2014.01.016

Boffetta, G., Lacorata, G., Redaelli, G., & Vulpiani, A. (2001). Detecting barriers to transport: A review of different techniques. *Physica D: Nonlinear Phenomena*, *159*, 58–70. https://doi.org/10.1016/S0167-2789(01)00330-X

Bosse, A., Fer, I., Lilly, J. M., & Søiland, H. (2019). Dynamical controls on the longevity of a non-linear vortex: The case of the Lofoten Basin Eddy. *Scientific Reports*, *9*, 1–13. https://doi.org/10.1038/S41598-019-49599-8

Carstensen, J., Weydmann, A., Olszewska, A., & Kwasniewski, S. (2012). Effects of environmental conditions on the biomass of *Calanus* spp. in the Nordic Seas. *Journal of Plankton Research*, *34*, 951–966. https://doi.org/10.1093/PLANKT/FBS059

Della Penna, A., De Monte, S., Kestenare, E., Guinet, C., & d'Ovidio, F. (2015). Quasi-planktonic behavior of foraging top marine predators. *Scientific Reports*, *5*, 1–10. https://doi.org/10.1038/SREP18063

De Monte, S., Cotté, C., d'Ovidio, F., Lévy, M., Le Corre, M., & Weimerskirch, H. (2012). Frigatebird behaviour at the ocean-atmosphere interface: Integrating animal behaviour with multi-satellite data. *Journal of The Royal Society Interface*, *9*, 3351–3358. https://doi.org/10.1098/RSIF.2012.0509

d'Ovidio, F., Fernández, V., Hernández-García, E., & López, C. (2004). Mixing structures in the Mediterranean Sea from finite-size Lyapunov exponents. *Geophysical Research Letters*, *31*, L17203. https://doi.org/10.1029/2004GL020328

Drouin, K. L., Mariano, A. J., Ryan, E. H., & Laurindo, L. C. (2019). Lagrangian simulation of oil trajectories in the Florida Straits. *Marine Pollution Bulletin*, *140*, 204–218. https://doi.org/10.1016/J.MARPOLBUL.2019.01.031

Enrile, F., Besio, G., Stocchino, A., Magaldi, M. G., Mantovani, C., Cosoli, S., et al. (2018). Evaluation of surface Lagrangian transport barriers in the Gulf of Trieste. *Continental Shelf Research*, *167*, 125–138. https://doi.org/10.1016/J.CSR.2018.04.016

Espinasse, B., Basedow, S. L., Tverberg, V., Hattermann, T., & Eiane, K. (2016). A major *Calanus finmarchicus* overwintering population inside a deep fjord in northern Norway: Implications for cod larvae recruitment success. *Journal of Plankton Research*, *38*, 604–609. https://doi.org/10.1093/PLANKT/FBW024

Espinasse, B., Tverberg, V., Basedow, S. L., Hattermann, T., Nøst, O. A., Albretsen, J., et al. (2017). Mechanisms regulating inter-annual variability in zooplankton advection over the Lofoten shelf, implications for cod larvae survival. *Fisheries Oceanography*, *26*, 299–315. https://doi.org/10.1111/FOG.12193

Falkenhaug, T., Tande, K., & Timonin, A. (1997). Spatio-temporal patterns in the copepod community in Malagen, Northern Norway. *Journal of Plankton Reserch*, *19*, 449–468. https://doi.org/10.1093/PLANKT/19.4.449

Fer, I., Bosse, A., & Dugstad, J. (2020). Norwegian Atlantic Slope Current along the Lofoten Escarpment. *Ocean Science*, *16*, 685–701. https://doi.org/10.5194/OS-16-685-2020

Fossheim, M., Zhou, M., Tande, K., Ole-Petter, P., Zhu, Y., & Edvardsen, A. (2005). Interactions between biological and environmental structures along the coast of northern Norway. *Marine Ecology Progress Series*, *300*, 147–158. https://doi.org/10.3354/MEPS300147

Gaardsted, F., Zhou, M., Pavlov, V., Morozov, A., & Tande, K. S. (2010). Mesoscale distribution and advection of overwintering *Calanus finmarchicus* off the shelf of northern Norway. *Deep Sea Research Part I*, *57*, 1465–1473. https://doi.org/10.1016/J.DSR.2010.07.003

Ghaffari, P., Isachsen, P. E., Nøst, O. A., & Weber, J. E. (2018). The influence of topography on the stability of the Norwegian Atlantic Current off northern Norway. *Journal of Physical Oceanography*, *48*, 2761–2777. https://doi.org/10.1175/JPO-D-17-0235.1

Haller, G. (2001). Lagrangian structures and the rate of strain in a partition of two-dimensional turbulence. *Physics of Fluids*, *13*, 3365–3385. https://doi.org/10.1063/1.1403336

Haller, G. (2002). Lagrangian coherent structures from approximate velocity data. *Physics of Fluids*, *14*, 1851–1861. https://doi.org/10.1063/1.1477449

Haller, G., & Yuan, G. (2000). Lagrangian coherent structures and mixing in two-dimensional turbulence. *Physica D: Nonlinear Phenomena*, *147*, 352–370. https://doi.org/10.1016/S0167-2789(00)00142-1

Halvorsen, E., Tande, K. S., & Høisæter, T. (1999). Physical and biological factors influencing the seasonal variation in distribution of zooplankton across the shelf at Nordvestbanken, northern Norway, 1994. *Sarsia*, *84*, 279–292. https://doi.org/10.1080/00364827.1999.10420432

Heath, M. R. (1999). The ascent migration of *Calanus finmarchicus* from overwintering depths in the Faroe-Shetland Channel. *Fisheries Oceanography*, *8*, 84–99. https://doi.org/10.1046/J.1365-2419.1999.00013.X

Helland-Hansen, B., & Nansen, F. (1909). The Norwegian Sea: Its physical oceanography based upon the Norwegian research 1900–1904. *Report on Norwegian Fishery and Marine Investigations*, *2*, 1–360.

Hu, Z. Y., & Zhou, M. (2019). Lagrangian analysis of surface transport patterns in the northern south China sea. *Deep Sea Research Part II*, *167*, 4–13. https://doi.org/10.1016/J.DSR2.2019.06.020

ICES oceanography data portal. (2012). ICES, Copenhagen.

Isachsen, P. E. (2015). Baroclinic instability and the mesoscale eddy field around the Lofoten Basin. *Journal of Geophysical Research: Oceans*, *120*, 2884–2903. https://doi.org/10.1002/2014JC010448

Kaartvedt, S. (1996). Habitat preference during overwintering and timing of seasonal vertical migration of *Calanus finmarchicus*. *Ophelia*, *44*, 145–156. https://doi.org/10.1080/00785326.1995.10429844

Koh, T. Y., & Legras, B. (2002). Hyperbolic lines and the stratospheric polar vortex. *Chaos*, *12*, 382–394. https://doi.org/10.1063/1.1480442

Lehahn, Y., d'Ovidio, F., Lévy, M., & Heifetz, E. (2007). Stirring of the northeast Atlantic spring bloom: A Lagrangian analysis based on multisatellite data. *Journal of Geophysical Research*, *112*, C08005. https://doi.org/10.1029/2006JC003927

Li, B., Zhou, L., Wang, C., Gao, C., Qin, J., & Meng, Z. (2020). Modulation of tropical cyclone genesis in the Bay of Bengal by the central Indian Ocean mode. *Journal of Geophysical Research: Atmospheres*, *125*, e2020JD032641. https://doi.org/10.1029/2020JD032641

Liu, B., D'Sa, E. J., & Joshi, I. D. (2019). Floodwater impact on Galveston Bay phytoplankton taxonomy, pigment composition and photo-physiological state following Hurricane Harvey from field and ocean color (Sentinel-3A OLCI) observations. *Biogeosciences*, *16*, 1975–2001. https://doi.org/10.5194/BG-16-1975-2019

Liu, Y., Wilson, C., Green, M. A., & Hughes, C. W. (2018). Gulf stream transport and mixing processes via coherent structure dynamics. *Journal of Geophysical Research: Oceans*, *123*, 3014–3037. https://doi.org/10.1002/2017JC013390

McClain, C. R. (2009). A decade of satellite ocean color observations. *Annual Review of Marine Science*, *1*, 19–42. https://doi.org/10.1146/annurev.marine.010908.163650

Melle, W., Runge, J., Head, E., Plourde, S., Castellani, C., Licandro, P., et al. (2014). The North Atlantic Ocean as habitat for *Calanus finmarchicus*: Environmental factors and life history traits. *Progress in Oceanography*, *129*, 244–284. https://doi.org/10.1016/J.POCEAN.2014.04.026

Ohman, M. D., Runge, J. A., Durbin, E. G., Field, D. B., & Niehoff, B. (2002). On birth and death in the sea. *Hydrobiology*, *20*, 55–68. https://doi.org/10.1023/A:1021228900786

Olascoaga, M. J., Beron-Vera, F. J., Brand, L. E., & Kocak, H. (2008). Tracing the early development of harmful algal blooms on the West Florida Shelf with the aid of Lagrangian coherent structures. *Journal of Geophysical Research*, *113*, C12014. https://doi.org/10.1029/2007JC004533

Olascoaga, M. J., Rypina, I. I., Brown, M. G., Beron-Vera, F. J., Koçak, H., Brand, L. E., et al. (2006). Persistent transport barrier on the West Florida Shelf. *Geophysical Research Letters*, *33*, L22603. https://doi.org/10.1029/2006GL027800

Opdal, A. F., & Vikebø, F. B. (2015). Long-term stability in modelled zooplankton influx could uphold major fish spawning grounds on the Norwegian continental shelf. *Canadian Journal of Fisheries and Aquatic Sciences*, *73*, 189–196. https://doi.org/10.1139/CJFAS-2014-0524

Planque, B. (2000). *Calanus finmarchicus* in the North Atlantic: The year of *Calanus* in the context of interdecadal change. *ICES Journal of Marine Science*, *57*, 1528–1535. https://doi.org/10.1006/JMSC.2000.0970

Prants, S. V., Budyansky, M. V., & Uleysky, M. Y. (2014). Identifying Lagrangian fronts with favourable fishery conditions. *Deep Sea Research Part I*, *90*, 27–35. https://doi.org/10.1016/J.DSR.2014.04.012

Runge, J. A., Plourde, S., Joly, P., Niehoff, B., & Durbin, E. (2006). Characteristics of egg production of the planktonic copepod, *Calanus finmarchicus*, on Georges Bank: 1994–1999. *Deep Sea Research Part II*, *53*, 2618–2631. https://doi.org/10.1016/J.DSR2.2006.08.010

Rypina, I. I., Kamenkovich, I., Berloff, P., & Pratt, L. (2012). Eddy-induced particle dispersion in the near-surface. *Journal of Physical Oceanography*, *42*, 2206–2228. https://doi.org/10.1175/jpo-d-11-0191.1

Sætre, R. (1999). Features of the central Norwegian shelf circulation. *Continental Shelf Research*, *19*, 1809–1831. https://doi.org/10.1016/S0278-4343(99)00041-210.1016/s0278-4343(99)00007-2

Sætre, R., & Ljøen, R. (1971). *The Norwegian coastal current*. Paper presented at Proceedings of the First International Conference on Port and Ocean Engineering under Arctic conditions. Technical University of Norway.

Sætre, R., & Mork, M. (1981). *The Norwegian coastal current*. Paper presented at Proceedings from the Norwegian Coastal Current Symposium. University of Bergen.

Saumweber, W. J., & Durbin, E. G. (2006). Estimating potential diapause duration in *Calanus finmarchicus*. *Deep Sea Research Part II*, *53*, 2597–2617. https://doi.org/10.1016/J.DSR2.2006.08.003

Scales, K. L., Hazen, E. L., Jacox, M. G., Castruccio, F., Maxwell, S. M., Lewison, R. L., & Bograd, S. J. (2018). Fisheries bycatch risk to marine megafauna is intensified in Lagrangian coherent structures. *Proceedings of the National Academy of Sciences*, *115*, 7362–7367. https://doi.org/10.1073/PNAS.1801270115

Shadden, S. C., Lekien, F., & Marsden, J. E. (2005). Definition and properties of Lagrangian coherent structures from finite-time Lyapunov exponents in two-dimensional aperiodic flows. *Physica D: Nonlinear Phenomena*, *212*, 271–304. https://doi.org/10.1016/J.PHYSD.2005.10.007

Skarðhamar, J., Slagstad, D., & Edvardsen, A. (2007). Plankton distributions related to hydrography and circulation dynamics on a narrow continental shelf off Northern Norway. *Estuarine, Coastal and Shelf Science*, *75*, 381–392. https://doi.org/10.1016/J.ECSS.2007.05.044

Slagstad, D., & Tande, K. S. (1996). The importance of seasonal vertical migration in across shelf transport of *Calanus finmarchicus*. *Ophelia*, *44*, 189–205. https://doi.org/10.1080/00785326.1995.10429847

Søiland, H., & Rossby, T. (2013). On the structure of the Lofoten Basin Eddy. *Journal of Geophysical Research: Oceans*, *118*, 4201–4212. https://doi.org/10.1002/JGRC.20301

Sundby, S. (1984). Influence of bottom topography on the circulation at the continental shelf off Northern Norway. *Fiskeridirektoratets skrifter, serie Havundersøkelser*, *17*, 501–519.

Sundby, S. (2000). Recruitment of Atlantic cod stocks in relation to temperature and advection of copepod populations. *Sarsia*, *85*, 277–298. https://doi.org/10.1080/00364827.2000.10414580

Tew-Kai, E., Rossi, V., Sudre, J., Weimerskirch, H., Lopez, C., Hernandez-Garcia, E., et al. (2009). Top marine predators track Lagrangian coherent structures. *Proceedings of the National Academy of Sciences*, *106*, 8245–8250. https://doi.org/10.1073/PNAS.0811034106

Toresen, R., Skjoldal, H. R., Vikebø, F., & Martinussen, M. B. (2019). Sudden change in long-term ocean climate fluctuations corresponds with ecosystem alterations and reduced recruitment in Norwegian spring-spawning herring (*Clupea harengus*, Clupeidae). *Fish and Fisheries*, *20*, 686–696. https://doi.org/10.1111/FAF.12369

Trodahl, M., & Isachsen, P. E. (2018). Topographic influence on baroclinic instability and the mesoscale eddy field in the Northern North Atlantic Ocean and the Nordic Seas. *Journal of Physical Oceanography*, *48*, 2593–2607. https://doi.org/10.1175/JPO-D-17-0220.1

von Appen, W.-J., Schauer, U., Hattermann, T., & Beszczynska-Möller, A. (2016). Seasonal cycle of mesoscale instability of the West Spitsbergen Current. *Journal of Physical Oceanography*, *46*, 1231–1254. https://doi.org/10.1175/JPO-D-15-0184.1

Weidberg, N., & Basedow, S. L. (2019). Long-term variability in overwintering copepod populations in the Lofoten Basin: The role of the North Atlantic oscillation and trophic effects. *Limnology & Oceanography*, *64*, 2044–2058. https://doi.org/10.1002/LNO.11168

Wei, X., Zhan, H., Cai, S., Zhan, W., & Ni, P. (2018). Detecting the transport barriers in the Pearl River estuary, Southern China with the aid of Lagrangian coherent structures. *Estuarine, Coastal and Shelf Science*, *205*, 10–20. https://doi.org/10.1016/J.ECSS.2018.03.010

Yu, L.-S., Bosse, A., Orvik, K. A., Bruvik, E. M., Hessevik, I., & Kvalsund, K. (2017). The Lofoten Basin eddy: Three years of evolution as observed by Seagliders. *Journal of Geophysical Research: Oceans*, *122*, 6814–6834. https://doi.org/10.1002/2017JC012982

Zhou, M., Tande, K. S., Zhu, Y., & Basedow, S. (2009). Productivity, trophic levels and size spectra of zooplankton in northern Norwegian shelf regions. *Deep Sea Research Part II*, *56*, 1934–1944. https://doi.org/10.1016/J.DSR2.2008.11.018

Zhu, Y., Tande, K. S., & Zhou, M. (2009). Mesoscale physical processes and zooplankton transport-retention in the northern Norwegian shelf region. *Deep Sea Research Part II*, *56*, 1922–1933. https://doi.org/10.1016/J.DSR2.2008